3D heat transfer, fluid flow and electromagnetic model for cold metal transfer wire arc additive manufacturing (Cmt-Waam)

S. Cadiou, M. Courtois, M. Carin, W. Berckmans, P. Le Masson

3D HEAT TRANSFER, FLUID FLOW AND ELECTROMAGNETIC MODEL FOR COLD METAL TRANSFER WIRE ARC ADDITIVE MANUFACTURING (CMT-WAAM)

S. CADIOU, M. COURTOIS, M. CARIN, W. BERCKMANS, P. LE MASSON
Univ. Bretagne Sud, UMR CNRS 6027, IRDL, F-56100 Lorient, France, e-mail: mickael.courtois@univ-ubs.fr

Abstract:

In this paper, we present a 3D numerical model of Wire Arc Additive Manufacturing to simulate the material deposition and the temperature field from the operating parameters. This predictive model, applied to a Cold Metal Transfer (CMT) process, takes into account electromagnetism, fluid flow and heat transfer in all domains (wire, arc, melt pool, substrate). This model, developed using COMSOL Multiphysics® software, calculates the creation of the molten metal drop at the filler wire tip, the detachment of the drop when the filler material retracts during the short circuiting phase and the growth of the deposit. This innovative work describes for the first time the wire behaviour dynamically and its interaction with the melt pool in 3D in a fully coupled approach. The dynamics of the free surface are treated with the level set method, particularly efficient for strong topological changes. The Lorentz forces, shear stress, arc pressure, and Joule effect are calculated. This model requires only the knowledge of the operating parameters without any assumption on the arc distribution. It aims to simulate the build-up of a 304 stainless steel wall. To validate this model, the melt pool dimensions and shape of the deposit calculated for the first layer are compared to experimental data given by macrographs and high speed videos.

Keywords : additive manufacturing; arc-wire; CMT; melt pool; numerical modelling; level set method; magnetohydrodynamics; heat transfer.

1. Introduction

The Cold Metal Transfer (CMT) process, developed by the Austrian company Fronius, arouses a growing interest in additive manufacturing. This process differs from GMAW process only by the type of mechanical droplet cutting method, resulting in an accurate control of material deposition and a low heat input. This process offers high arc stability and material transfer without spatters, leading to better quality parts. This material deposition process is carried out in four steps. The first step consists in melting the tip of the fusible electrode with the presence of the arc. During the second step, the wire goes down in contact with the substrate having in its tip a droplet of liquid metal. A short circuit then occurs and the arc is extinguished. In the third step, the droplet is detached from the wire as it rises due to the surface tension. Finally, the fourth step consists in starting the arc again to restart the material supply cycle. So the metal transfer process during CMT is particularly complex involving not only a multiphysics coupling between electromagnetic effect, fluid flow, heat and mass transfer but also phase transfer and strong interface topological changes.

However, there are very limited numerical multiphysics studies in 3D to simulate multilayer deposition such as in WAAM processes. In addition, numerical models dealing with the CMT process are less common and do not treat all the whole process of metal transfer. One of the reasons is the prohibitive computing times. In order to reduce computation times, these models are generally simplified and based on empirical laws requiring a calibration of input parameters with experimental data. In order to avoid this tedious calibration, there is a need to develop multiphysics model describing all the physical phenomena in the arc with the detachment of droplets and their transfer into the melt pool. In the literature, the most complete models have been realized in 2D axisymmetric. Moreover, such works have focused on models simulating Gas Metal Arc Welding (GMAW) rather than

Wire Arc Additive Manufacturing (WAAM). With such 2D axisymmetric model, it is possible to simulate the growth of droplets, its detachment from the wire tip and the transfer of the droplet through the arc plasma, as done by Jones et al. [1-2] with a simplified treatment of the electromagnetic forces, or by Fan and Kovacevic [3] with a more complete model using the Volume of Fluid (VOF) method to track free interface motion. The numerical work performed by Hu and Tsai [4-5] has highlighted the influence of the moving droplets on the current, temperature, velocity and pressure distributions in the arc column. Their calculations question the common assumption of a Gaussian distribution for arc pressure, current, and heat flux at the melt pool surface. Such models are also used to analyse different effects such as the transition from globular to spray transfer [6-7], the influence of electrode polarity [8], the influence of types of current waveforms [9-10], or the influence of shielding gas on the detachment of droplets [11-12].

Nevertheless, a limited number of 3D models are present in the literature simulating the WAAM process. These 3D models can be divided into two major categories: those that simulate the complete build-up at “part scale” and those that simulate at “melt pool scale”. The main issue is that a complete 3D modelling has to face prohibitive calculation times. In order to reduce computation times, these models are generally simplified and based on empirical laws requiring a calibration of input parameters with experimental data or numerical data with models simulating at the “melt pool scale”. The droplet formation and detachment, droplet flight in an arc plasma and impingement of droplets are not explicitly simulated.

Bai [13] proposed a 3D heat transfer and fluid flow model to simulate multilayer deposition of plasma arc welding (PAW). This model is used to simulate the 1st, 2nd and 21st layer depositions. However, due to prohibitive computation time, the simulation of the 21st layer is initialised with the experimental profile of the 20th layer.

Ogino et al. [14] developed a similar multi-layer 3D model to analyse the influence of the deposit strategy and cooling condition for a CMT process. Note that their model is simplified in terms of heat input and arc pressure. A VOF method is used to track the melt pool surface. However, the geometry of the deposition is not fully consistent with the experiments. But the numerical results show a similar trend with respect to the conditions used. Therefore, this kind of model can help to find adequate operating parameters for the build-up of high quality parts.

Hejripour [15] has also proposed a heat transfer and fluid flow model to simulate a WAAM process. An Arbitary Lagrangian-Eulerian (ALE) method is used to predict the shape of material deposit but his approach is limited to one layer.

All the aforementioned 3D models need calibration to find the values of the Gaussian functions that give the best match between numerical and experimental weld zone profiles. In order to avoid this tedious task, some authors have developed complete 3D models describing all the physical phenomena in the arc with the detachment of droplets and their transfer into the melt pool.

Xu et al. [16] developed a three-dimensional model for the plasma arc and metal transfer in GMAW using a VOF method. Because of the very long calculation times, they made simplifications at the interface of the metal and the plasma arc. Moreover, the deposition was not simulated. Their model was able to simulate a moving arc case. From their results, they concluded that the time-invariant Gaussian assumption for the distributions of the arc pressure, heat flux, and current density on the workpiece surface is questionable.

Zhou et al. [17] developed a three-dimensional weakly coupled model to simulate the additive manufacturing process. A first magneto-thermohydraulic model is realized to obtain the electromagnetic forces, the plasma shear stress, the arc pressure, and the net heat flux. These results are used as input data for a thermohydraulic model simulating the deposition. This second model takes into account the droplet fall in the melt pool. The drops are assumed to be spherical at a temperature of 2100 K, based on results from the literature. This model calculates the temperature field and morphology of molten pool. The authors

obtained consistent results with experimental data in terms of molten pool morphology and cross-section profile.

In this paper, we propose a 3D model to simulate a CMT-WAAM process, where the detachment of the material is induced by the retraction of the wire. This configuration was not yet considered in the literature. This work represents a straight continuation of our previous 2D axisymmetric model [18]. This 3D model, developed with Comsol Multiphysics® software version 5.4, describes the four steps to metal transfer during CMT. The model simulates the forward and backward motion of the filler wire. It also predicts its impingement into the melt pool, the growth of the melt pool and the formation of the deposited bead. It is based on the computation of magnetothermal-hydrodynamic equations in all domains (wire, arc, melt pool, substrate) with the level set method for the interface tracking. The CMT model is used to simulate the build-up of a wall in a 3D configuration. This multiphysics model is limited to the scale of the melt pool but allows to study the arc and melt-pool dynamics. This model requires only the knowledge of the operating parameters without any assumption on the arc distribution, to predict the temperature and fluid velocity fields in the melt pool during material deposition as well as its geometry. However, in order to reduce the computation time, some simplifications are made and explained in the next section.

2. Modelling of the CMT process

The 3D multiphysics model presented in this section aims to simulate all the physical phenomena in the wire, the arc and the molten pool. It has been developed on the basis of the 2D axisymmetric model presented in [18], but with adjustments to take into account the specificities of the CMT process. The simulated configuration and the associated boundary conditions are defined by the instrumented tests presented in section 3. In order to reduce the computation time, the geometry of the computational domain is limited to an area around the melt pool, in which the MIG torch axis is assumed to be fixed and the substrate is assumed to be moving.

The mathematical description is similar to the 2D axisymmetric multiphysics model, including Maxwell's equations, mass continuity, momentum conservation, energy equation and a level set approach. The main differences are to be found in the wire which, in the case of the CMT process, performs forward and backward movements with periods of contact with the melt pool. The arc length therefore varies continuously.

2.1. Assumptions

To reduce the complexity of the modelling effort, some assumptions have been made for the arc and the metal transport simulation. These assumptions, commonly used [12-14, 18], are listed below:

- The plasma is in local thermodynamic equilibrium (LTE), which means that all species of particles (ions, neutrons, electrons) are considered at the same temperature. This assumption is quite appropriate in the arc column, but is not verified in the anode and cathode sheaths. To avoid the development of a twin temperature model (electrons and ions), some authors use the conductive layers method [19-20], which consists in defining, in the plasma, thin layers adjacent to the electrodes, with an electrical conductivity equal to that of the electrodes instead of the gas. However, in the present work, the level set method is used to represent the interface between the electrodes and the gas. This method introduces a smooth change of the properties at the interface. So, it is not necessary to introduce a method such as the conductive layers method. In addition, note that specific interfacial conditions are also considered in order to deal with the complex electrical phenomena within the sheath (Eq 17-20). The molten and solid regions of the metal are treated as liquid phase, the arc plasma

is considered as gaseous phase. These two phases are assumed to be immiscible, incompressible and Newtonian fluids in a laminar flow.

- The Marangoni convection is neglected, meaning that a constant surface tension coefficient is considered for a sake of simplicity. Although such an assumption may seem questionable, especially with regard to the experimental work done by [21] for a CMT process, the Marangoni effect can be a tough challenge to model since the thermocapillary coefficient, strongly dependent on the chemical composition of wire and shielding gas, is difficult to measure precisely.

- Buoyancy force is taken into account using the Boussinesq approximation.

- The effect of metal vapours coming from the evaporation at the melt pool surface is not included in the model [8, 18, 19, 22, 23].

- In the arc column, the electron enthalpy is not considered here based on [20, 24]. This effect is formulated usually by the following expression $div\left(\frac{5}{2}\frac{k_b}{e}\,T\vec{J}\right)$ in the energy equation, where k_b represents the Bolzmann's constant and e the elementary charge. Using the model, this term was estimated to be less than 5% of the Joule effect term.

2.2. Level set approach

In order to simulate the metal transfer, the level set method [25] is chosen to track the moving interface between the shielding gas and the metal phase. The wire, the substrate and the molten metal are treated as a unique metal phase. The level set method enables to simulate the dynamic shape of the wire tip, the detachment of the droplet during wire retraction, and the dynamic shape of the deposit during material addition. Although the VOF method is more often used for this kind of simulations, the finite element software COMSOL Multiphysics was chosen here. This software does not include the VOF method, which is proposed rather by finite volume softwares, dedicated to CFD simulations. In addition, the level set method has been used with success in previous works [18, 26].

A ϕ variable, defined in the gas and metal ranges from 0 to 1. It is arbitrarily equal to 0 in gas and 1 in metal. The isovalue $\phi = 0.5$ represents the interface gas-metal. A smoothed step function makes it possible to vary gradually the ϕ variable from one phase to another.

The ϕ variable is also used to apply the adequate properties in gas and metal using a unique formulation, expressed as follows:

$$\alpha = \alpha_{gas} + (\alpha_{metal} - \alpha_{gas})\phi \qquad (1)$$

where α_{gas} and α_{metal} represent the values of a given physical property in both phases. These properties can be temperature-dependent. With such a formulation, an average value for the material properties is assigned at the interface gas-metal.

The interface has to be transported with the fluid velocity, so the following transport equation is solved [27]:

$$\frac{\partial \phi}{\partial t} + \vec{v}.\overrightarrow{grad}(\phi) = \gamma_{ls}\,\overrightarrow{div}\left(\varepsilon_{ls}\,\overrightarrow{grad}(\phi) - \phi(1-\phi)\frac{\overrightarrow{grad}(\phi)}{|\overrightarrow{grad}(\phi)|}\right) \qquad (2)$$

where γ_{ls} and ε_{ls} are, respectively, a reinitialisation speed (m/s) and the interface thickness controlling parameters (m). The right hand-side allows the reinitialisation of the level set

function avoiding numerical instability [27-29]. A more detailed explanation of this method is given in reference [18].

A Dirac delta function $\delta(\phi)$ is used to assign the interfacial conditions as source terms in the conservation equations [18]. This function is non-zero only in the vicinity of the gas-metal interface.

2.3. Electromagnetism

The electromagnetic problem is solved using the current continuity equation and Ohm's law from Maxwell's equations :

$$\begin{gathered} div\left(\sigma_e \overrightarrow{grad}(V) + \sigma_e \frac{\partial \vec{A}}{\partial t}\right) = 0 \\ \sigma_e \frac{\partial \vec{A}}{\partial t} + \frac{1}{\mu_0} \overrightarrow{rot}\left(\overrightarrow{rot}(\vec{A})\right) + \sigma_e \overrightarrow{grad}(V) = \vec{0} \end{gathered} \tag{3}$$

where σ_e is the electrical conductivity, V is the electrical potential, μ_0 is the magnetic permeability and $\vec{A}$ is the magnetic vector potential.

2.4. Conservations of mass and momentum

The conservation of mass and momentum equations are solved in the gas and liquid metal and can be expressed as follows:

- Mass Conservation

$$div(\vec{v}) = 0 \tag{4}$$

where $\vec{v}$ is the velocity vector. To avoid convergence issues due to the drastic change of density at the interface gas-metal, the continuity equation is formulated for incompressible fluids in the entire domain.

- Conservation of momentum

$$\rho\left(\frac{\partial \vec{v}}{\partial t} + \overline{\overline{grad}}(\vec{v}).\vec{v}\right) = \overrightarrow{div}\left[-P\bar{\bar{\imath}} + \mu_f\left(\overline{\overline{grad}}(\vec{v}) + {}^t\overline{\overline{grad}}(\vec{v})\right)\right] + \overrightarrow{F_v} \tag{5}$$

where P is the pressure, $\bar{\bar{\imath}}$ the identity matrix, μ_f the dynamic viscosity and $\overrightarrow{F_v}$ the volume force expressed as follows:

$$\vec{F}_v = \vec{F}_{mag} + \vec{F}_{gravity} + \vec{F}_{surface\ tension} + \vec{F}_{Darcy} \tag{6}$$

- *Electromagnetic force*

$$\vec{F}_{mag} = \vec{j} \times \vec{B} \tag{7}$$

where B is the magnetic flux density and j is the current density calculated by the Maxwell's equations.

- *Gravity*

$$\vec{F}_{gravity} = \rho \vec{g} \tag{8}$$

where ρ is the density and $\vec{g}$ is the acceleration due to gravity.

- *Surface tension*

The surface tension acting at the gas-metal interface is modelled by a localized volume force $\vec{F}_{surface\ tension}$, since, with the level set method, all the interfacial forces are integrated

in the momentum equation as volume force by multiplying the surface force (in $N.m^{-2}$) by a Dirac delta function (δ in m^{-1}). The surface tension is computed, according to [30] by the expression :

$$\vec{F}_{surface\ tension} = (\vec{n}\kappa + (I - \vec{n}.\vec{n}^T)\nabla)\gamma)\ \delta(\phi) \quad (9)$$

where κ is the curvature, γ is the surface tension coefficient.

- *Darcy*

To treat the solid-liquid mushy zone in the metal and the solid, two types of flow extinction methods are used. The first one uses a very large value of viscosity to supress the velocity in the solid part. The following expression for the metal viscosity is then chosen:

$$\mu = \mu_{metal_{liquid}}\, f_L + \mu_{metal_{solid}}(1 - f_L) \quad (10)$$

where $\mu_{metal_{solid}}$ = 1000 Pa.s, $\mu_{metal_{liquid}}$ is the dynamic viscosity of liquid metal and f_L is the liquid fraction function. This function is assumed, through a simple model, to vary linearly with temperature in the mushy zone as follows:

$$f_L = \begin{cases} 1 & \text{if } T > T_L \\ \dfrac{T - T_S}{T_L - T_S} & \text{if } T_S \leq T \leq T_L \\ 0 & \text{if } T < T_S \end{cases} \quad (11)$$

where T is the temperature, T_S and T_L are, respectively, the solidus and liquidus temperatures of the workpiece material.

In addition, to stiffen the wire during forward and backward movements for the solid part of the wire, a Darcy condition $\vec{F}_{Darcy}$ is added in the form:

$$\vec{F}_{Darcy} = -C\frac{(1 - f_L)^2}{f_L^3 + b}\begin{pmatrix} v_x \\ v_y \\ 0 \end{pmatrix}_{(\vec{x},\vec{y},\vec{z})} \quad (12)$$

where C is a relatively huge constant that ensures the decrease of the velocity field in the solid region, b is a relatively low constant introduced to avoid division by zero. v_x and v_y the components of the velocity vector $\vec{v}$. Having a z-component equal to zero makes the wire move only along the $\vec{z}$ axis. Darcy's law has not been applied in the substrate because the formulation must be changed (with the moving velocity of the substrate instead of the wire) and locally within the contact area of the wire and the substrate, two formulations of Darcy's law cannot coexist.

2.5. Conservation of energy

The energy conservation is governed by the following equation:

$$\rho C_p^{eq}\left(\frac{\partial T}{\partial t} + \vec{v}.\overrightarrow{grad}(T)\right) = div\left(\bar{\bar{k}}\,\overrightarrow{grad}(T)\right) + S_v \quad (13)$$

where ρ is the density, C_p^{eq} is an equivalent specific heat, that equals C_p in the arc-plasma domain, and is modified to $C_p + L_f\,\frac{df_L}{dT}$ in the metal domain to account for the latent heat of fusion L_f, k is the thermal conductivity, T is the temperature, and S_v is a volumetric heat source term expressed by:

$$S_v = S_{Joule\ effect} + S_{rad} + S_{cathode/plasma\ interface} + S_{anode/plasma\ interface} + S_{level\ set} \quad (14)$$

The terms of this equation are detailed as follows :

- *Joule effect* [18]

$$S_{Joule\ effect} = \vec{j}.\vec{E} \quad (15)$$

where $\vec{j}$ is the current density calculated with the relation $\vec{j} = \sigma_e \vec{E}$ and $\vec{E}$ is the electric field calculated with the relation $\vec{E} = -\overrightarrow{grad}(V) - \frac{\partial \vec{A}}{\partial t}$. The variables V and $\vec{A}$ are directly calculated from electromagnetic equations.

- *Radiation of the plasma* [18]

The term S_{rad} represents the radiation losses in the plasma.

$$S_{rad} = -4\pi\varepsilon_N \quad (16)$$

where ε_N is the net emission coefficient of Argon taken from [31].

- *Cathode/plasma interface*

$$S_{cathode/plasma\ interface} = (j_i V_i - j_e \phi_c)\delta(\phi) \quad (17)$$

where j_e is the electron current density at the surface of the cathode and ϕ_c the work function of the electrode wire [31]. This current density cannot exceed the thermionic current density determined by the Richardson-Dushmann equation [31]

$$j_{em} = A_r T^2 \exp\left(-\frac{e\phi_e}{k_B T}\right) \quad (18)$$

where A_r is the Richardson's constant, T is the temperature, e is the elementary charge, ϕ_e is the cathode effective work function and k_B is the Boltzmann constant.

The term $j_i V_i$, represents the ionisation energy, where j_i is the ion current density and V_i the ionisation potential of the gas. It is assumed that if the calculated current density is greater than the current density emitted by thermionic emission, the additional current density is then provided by the ions transferred from the plasma to the cathode. This ion current density is then expressed as follows [31]:

$$j_i = \begin{cases} j_c - j_{em} & if\ j_c - j_{em} > 0 \\ 0 & if\ not \end{cases} \quad (19)$$

As in [20], it is considered that the normal component of $\vec{j}$ at the surface is preponderant so it is stated: $j_c = |\vec{j}.\vec{n}|$.

- *Anode/plasma interface*

At the surface of the wire, which represents the anode, the heating induced by the absorption of electrons is taken into account through the following expression:

$$S_{anode/plasma\ interface} = (|\vec{j}.\vec{n}_a|\phi_a)\delta(\phi) \quad (20)$$

where ϕ_a is the anode work function.

- *Level set adaptation*

The term $S_{level\ set}$ is introduced to overcome some of the disadvantages inherent in the level set method. At the interface, due to the transition, the mixed thermophysical properties prevent an appropriate amount of heat transfer between the metal and the arc. To solve this problem, a Gaussian heat source is introduced. The power of this source is directly calculated by the model via the Joule effect term. The distribution parameter r_0 is taken equal to the diameter of the filler wire. This artifice is already discussed in details in [18].

$$S_{level\ set} = \begin{cases} \frac{e^{-\frac{r^2}{r_0^2}}}{\pi r_0^2} \int_V S_{Joule\ effect} dV\ \delta(\phi) & at\ the\ wire/plasma\ interface \\ \frac{e^{-\frac{r^2}{r_0^2}}}{\pi r_0^2} \int_V S_{Joule\ effect} dV\ \delta(\phi) & at\ the\ substrate/plasma\ interface \end{cases} \quad (21)$$

2.6. Computational domain and boundary conditions

This multiphysics 3D model aims to analyse the physical phenomena in the vicinity of the arc and the melt pool, so the geometry of the computational domain is reduced, which also allows to limit calculation time (Fig. 1). For similar reasons, the computational domain has been divided in several domains in which the equations are not all solved. The energy conservation equation is solved in all domains, but the level set and momentum equations are not solved in the lower part of the substrate (domain 1). Maxwell's equations are solved only in domains 2, 3, 4, 5 and the wire domain since the electromagnetic effects are negligible in the other domains. The initial conditions are:

- For the energy problem: T_{init} = 293 K
- For the electromagnetic problem: A = 0 Wb/m and V = 0 V
- For the fluid problem: u, v, w = 0 m/s and p = 0 Pa
- For the level set problem: Φ = 1 in domains 2 and 7. Φ = 0 in domains 3 to 6.

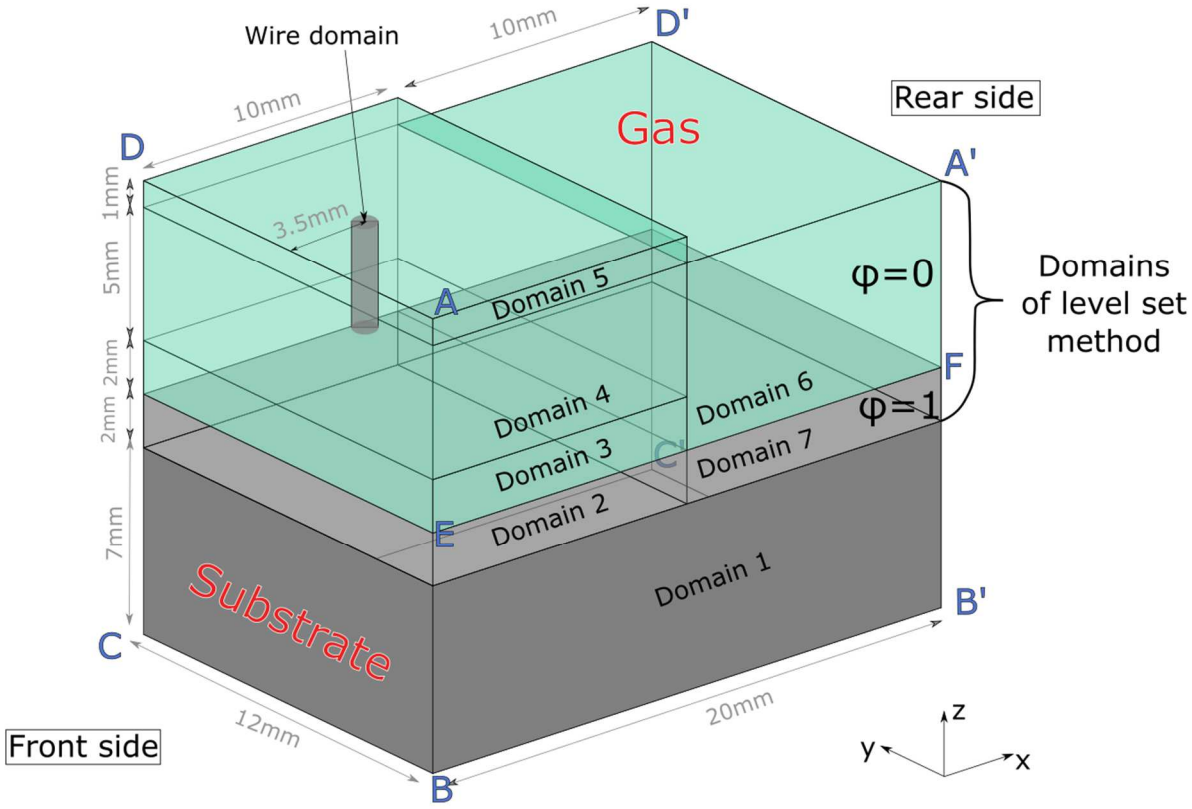

Fig. 1 - Geometry of the computational domains (dimensions in mm)

	ABCD	AA'FE	ADD'A'	Wire inlet	EFB'B	A'B'C'D'	BB'C'C

		(and its symmetry)	(except wire)		(and its symmetry)		
T	T = 300 K	$\vec{q}.\vec{n} = 0$	$\vec{q}.\vec{n} = 0$	T = 300 K	Eq. 23 and 24	$\vec{q}.\vec{n} = 0$	Eq. 23 and 24
(u, v, w, p)	$v_{substrate}$	$\vec{v} = \vec{0}$	$p = p_0$	v_{wire}	$\vec{v} = \vec{0}$	$p = p_0$	
$(V, \vec{A})$	$\vec{j}.\vec{n} = 0$ $\vec{A} \times \vec{n} = \vec{0}$	$\vec{j}.\vec{n} = 0$ $\vec{A} \times \vec{n} = \vec{0}$	$\vec{j}.\vec{n} = 0$ $\vec{A} \times \vec{n} = \vec{0}$	$I = \int_{\partial\Omega} -\vec{n}.\vec{j}\, d = 25\ A$	$\vec{j}.\vec{n} = 0$ $\vec{A} \times \vec{n} = \vec{0}$	$\vec{j}.\vec{n} = 0$ $\vec{A} \times \vec{n} = \vec{0}$	$V = 0\ V$

Table 1 - Boundary conditions

The boundary conditions used for the thermal problem are the following:

- A temperature of 300 K is prescribed at the surfaces normal to the $\vec{x}$ axis, front side, of the domains 1, 2, 3, 4, and 5.
- For the open boundary of the plasma domains (domains 3, 4, 5 and 6 (Fig. 1)), the outflow condition of Comsol Multiphysics software is chosen, which is equivalent to an insulation condition:

$$\vec{q}.\vec{n} = 0 \tag{22}$$

- Radiation and convection losses are applied to the surfaces of the substrate (domains 1 and 2 (Fig. 1)). The convection losses are calculated from:

$$q_c = -h_c(T - T_{amb}) \tag{23}$$

where h_c is a convective heat transfer coefficient and T_{amb} is ambient temperature.

The radiation losses are determined from:

$$q_r = -\varepsilon\sigma_B\left(T^4 - T_{amb}^4\right) \tag{24}$$

where ε is the metal emissivity, σ_B is the Stefan-Boltzmann constant and T is the temperature at the metal surface.

For the fluid flow problem, which is solved in all the domains except domain 1 (Fig. 1), the boundary conditions are:

- An inlet velocity is prescribed at the surfaces normal to the x-axis, front side of the domains 1, 2, 3, 4, and 5 (Fig. 1). This velocity corresponds to the torch transverse speed.
- A relative pressure equal to zero is set at the surface normal to the x-axis, rear side, of domains 5 and 6, but also at the upper surface of domain 6 (Fig. 1).
- At the side surfaces, a sliding condition is prescribed, $\vec{v}.\vec{n} = 0$ m.s^{-1}, thus allowing the domains to be able to translate at the torch speed.
- At the upper surface of the wire domain, a wire feed speed is applied. This velocity can be positive or negative to represent the forward and backward movement. In order to control the wire direction, the development of the model was based on the value of the voltage. Indeed, the voltage becomes zero when the electrode wire tip comes in contact with the melt pool and short-circuiting occurs. However, the wire retracting movement is repeated at a specific frequency. Being aware of these elements, the wire speed was managed in the model as follows. First, a negative velocity is prescribed to the wire until the voltage becomes zero, which means that the wire tip makes contact with the molten pool. Then at the time of the short circuit, a positive velocity for a half-period is prescribed to simulate the wire retracting movement. At the end of the half-period, the cycle repeats, that is to say that the wire descends until the voltage becomes again zero. The wire retracting frequency is set to 15 Hz, corresponding to the value measured by high speed camera.

- At the upper surface of domain 5 (Fig. 1), the shielding gas, entering a nozzle with an internal diameter of 14 mm, is taken into account by applying a normal inlet speed to the surface equal to 0.25 $m.s^{-1}$.

Boundary conditions related to the electromagnetic problem, which is solved only in domains 2, 3, 4, 5, and wire (Fig. 1), are defined as follows:

- The electric current is taken constant, and equal to 25 A, in order to simplify the model. It is applied to the upper surface of the filler wire area.
- A zero voltage is prescribed at the lower surface of the substrate, domain 2 (Fig. 1).

All the boundary conditions are summarized in Table 1 for a better clarity.

The material properties are given in Table 2. Pure argon is used for shielding gas. The wire electrode and substrate are composed of 304 stainless steel.

	304 stainless steel	**Argon**
Thermal conductivity k ($W.m^{-1}.K^{-1}$)	$k(T)$ [32]	0.08
Specific heat c_p ($J.kg^{-1}.K^{-1}$)	$C_p(T)$ [32]	510
Density ρ ($kg.m^{-3}$)	7000	1
Dynamic viscosity μ_f (Pa.s)	0.001	0.1
Electrical conductivity σ_e ($S.m^{-1}$)	7.7×10^5 [33]	$\sigma_e(T)$ [34]
Magnetic permeability μ_0 ($H.m^{-1}$)	$4\pi \times 10^{-7}$ [7]	
Liquidus temperature T_l (K)	1723 [35]	
Solidus temperature T_s (K)	1673 [35]	
Melting temperature T_{fusion} (K)	1700 [35]	
Net emission coefficient ε_N ($W.m^{-3}.ster^{-1}$)		$\varepsilon_N(T)$ [19]
Surface tension coefficient γ ($N.m^{-1}$)	1.6 [19]	
Anode work function ϕ_a (V)	4.65 [24]	
Cathode work function ϕ_c (V)	4.65 [24]	
Effective work function ϕ_e (V)	2.63 [24]	
Richardson's constant A_r ($A.m^{-2}.K^{-2}$)	3×10^4 [24]	
Ionisation potential V_i (V)	15.68 [24]	
Level set reinitialisation speed γ_{ls} (m/s)	5	
Level set interface thickness ε_{ls} (μm)	90	

Table 2 – Material properties and parameters

2.7. Mesh

Three-dimensional models are known to be computationally expensive, especially when the solved equations require a fine mesh. But the mesh requirement varies according to the physics. In the case of the WAAM-CMT process, the most demanding equation is that linked to the level set method. Indeed, in order to track the strong topological changes of the interface during all the metal transfer process, a fine mesh is required in a large part of the computational domain. A convergence study has shown that a mesh with a minimum size of 180 µm is necessary to properly handle the displacement of the interfaces. However, a such fine mesh is not needed for the other physics. So, to reduce computation times, coarser mesh is used for the other equations, as proposed by Courtois et al. [26]. This technique, applied to laser welding, has thus enabled a drastic reduction in calculation times, decreasing from 4 weeks to just one day. Here, a mesh of 500 µm is chosen for the other physics. Projection coupling variables are defined to interpolate the different solutions from one mesh to another and thus perform all the couplings at all time steps. All the calculations are realized with a computational domain meshed using standard linear triangular elements.

Computations are performed within 15 days, to simulate 6 s of process, on 7 cores (3.20GHz) and require around 30 GB RAM (DDR4). A constant time step of 10^{-4} s is used.

3. Results and discussion

3.1. Experimental data

The present simulations have been based on experimental data carried out at the Institut des Matériaux Jean Rouxel (IMN) in Nantes (France). The experiment consists in the build-up of a wall of five layers. The deposition direction alternates between layers, as shown in Fig. 2. The substrate is made of 304 stainless steel and is 130 mm long by 12 mm wide and 50 mm high. The built part was manufactured using a filler wire also in stainless steel 304 of 1 mm in diameter. The operating parameters chosen for the multiplayer deposits are as follows:

- the travel speed of the torch is 30 cm / min,
- the flow rate of argon gas is 15 L / min,
- the average speed of the filler wire is 3.5 m / min. Since the CMT system used does not provide an accurate measurement of the instantaneous wire speed during its forward and backward movements, an average speed was determined from a mass balance of deposited material. Indeed, the macrographs realized on the wall for two layers make it possible to estimate the volume of deposited material. By taking into account the deposition duration of 20 s, it is possible to estimate the average wire feed speed.

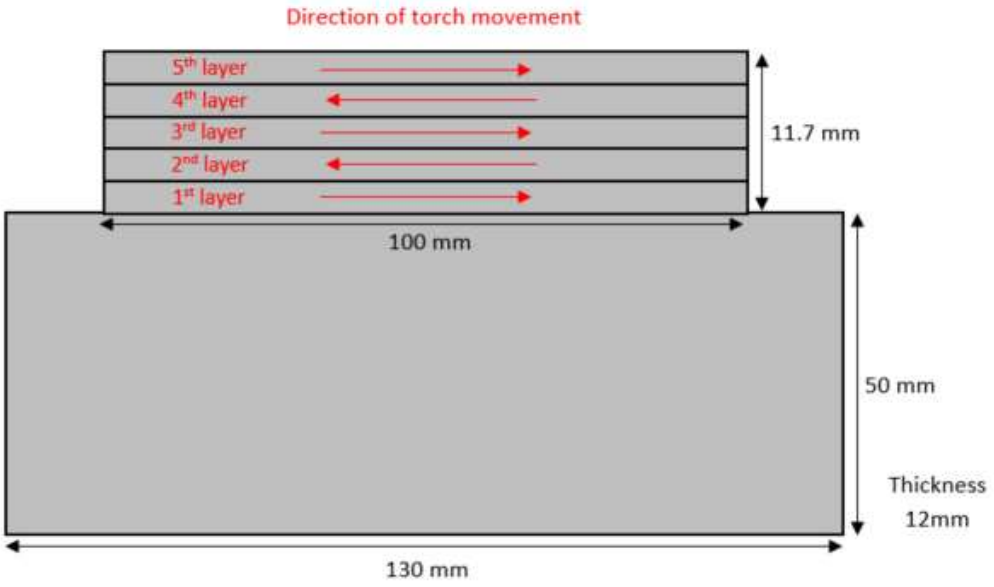

Fig. 2 – CMT multiplayer procedure consisting of 5 layers of 304 stainless steel deposited on a substrate of the same material

During the experiment, a high speed camera (Keyence VM-600M) was used to visualise the melt pool and its interaction with the filler wire. The high-speed camera has been combined with laser lighting to improve the visibility of the melt pool and limit disturbances from the electric arc. The videos are made with an acquisition frequency of 2000 Hz and allow to measure the length of the melt pool and its height for the different layers (Fig. 3). The high speed camera is positioned perpendicular to the wall and is focused at the middle of the wall so that the dimensions of the melt pool can be viewed in the longitudinal plane.

The vertical position of the camera has been adjusted between each layer so that it is always centred on the melt pool of each layer during their build-up.

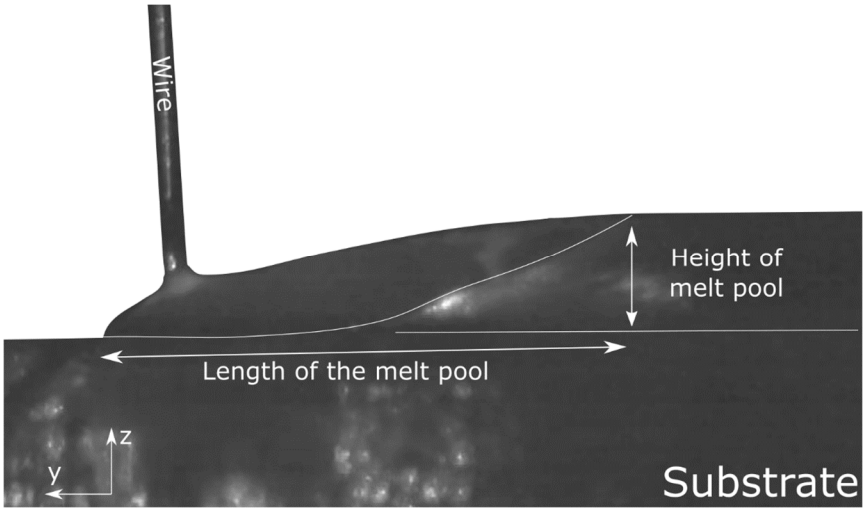

Fig. 3 - Picture from the high-speed camera illustrating the measurement of the length and height of the melt pool

3.2. Simulation results

The model is used to analyse the first stages of the metal transfer during a WAAM-CMT process. To start the electric arc in the model, it was necessary to define an electrically conductive zone in the argon domain between the wire and the substrate for a short duration of 10 ms, the time to initiate the electric arc. After arc ignition, the argon domain regains its electrical conductivity as a function of temperature. This first step is necessary since argon is not an electrical conductor at ambient temperature, but this step is no longer required for the other cycles. Indeed, the temperature along the z-axis remains sufficient high to have an electrically conductive area to enable the reignition of the arc for the following cycles. Fig. 4 shows the temperature field in the wire and the melt pool at different times. The illustrations show the first moments of the process with the addition of two droplets. At t = 0.08 s, it is observed the first drop forming at the tip of the wire. At t = 0.19 s, the wire descends until it touches the substrate. From this moment, the speed of the feed wire reverses so that it can go up. At t = 0.22 s, it can be seen that the shape of the wire tip changes from oblate to a pointed bevelled shape. The liquid metal bridge is broken due to surface tension effect, leading to the detachment of the droplet. At t = 0.26 s, the detached droplet spreads over the substrate. At the same time, the arc is re-ignited, that heats and melts the wire tip, and a new droplet is formed at the electrode tip. At t = 0.28 s, the wire is fed forward once more, the new droplet grows to restart a new supply cycle as it can be seen from 0.34 to 0.40 s. The last three illustrations show the growth of the melt pool during several cycles and, therefore, the evolution of the deposit at t = 1.5 s, 3 s and 4.5 s. For a better understanding of the dynamic behaviour, see [video1].

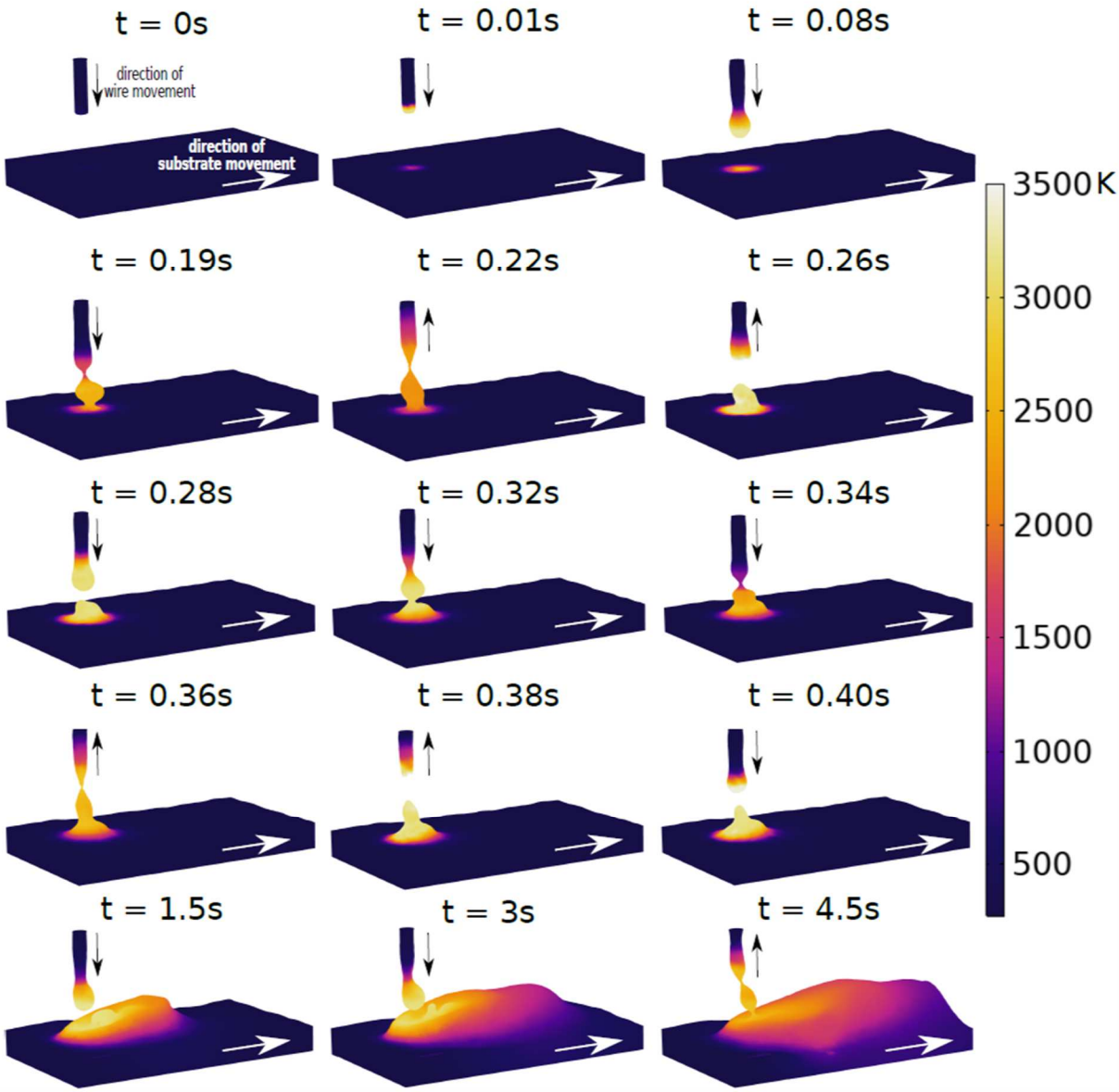

Fig. 4 – Sequence of temperature fields (in K) during the detachment of the first two droplets (from t = 0 to 0.4 s) as well as the growth of the melt pool during the build-up of the wall (from t = 1.5 to 4.5 s). The black arrow indicates the direction of the wire and the white one indicates the relative motion of the substrate

The model also makes it possible to provide information concerning the flow in the liquid metal. This information is used to analyse the heat transfer and momentum of the droplet in the melt. Fig. 5 highlights that, during the impact of the droplet in the molten bath, the flows are directed towards the bottom of the melt pool at first, then mainly towards the rear of the fusion bath. Consequently, the addition of the droplet promotes the penetration of the molten bath into the substrate. The study of the flow therefore makes it possible to visualise the energy transfer from the droplet to the melt pool and thus better understand the penetration of the bead into the substrate. The numerical results show that the maximum flow velocities are concentrated at the location of the impact of the droplet and are approximately 0.07 $m.s^{-1}$. In the front part of the melt pool, the fluid velocities are significantly lower, and are of the order of 0.01 $m.s^{-1}$. From the velocity vector field in the wire, it can be noticed the direction of the wire movement.

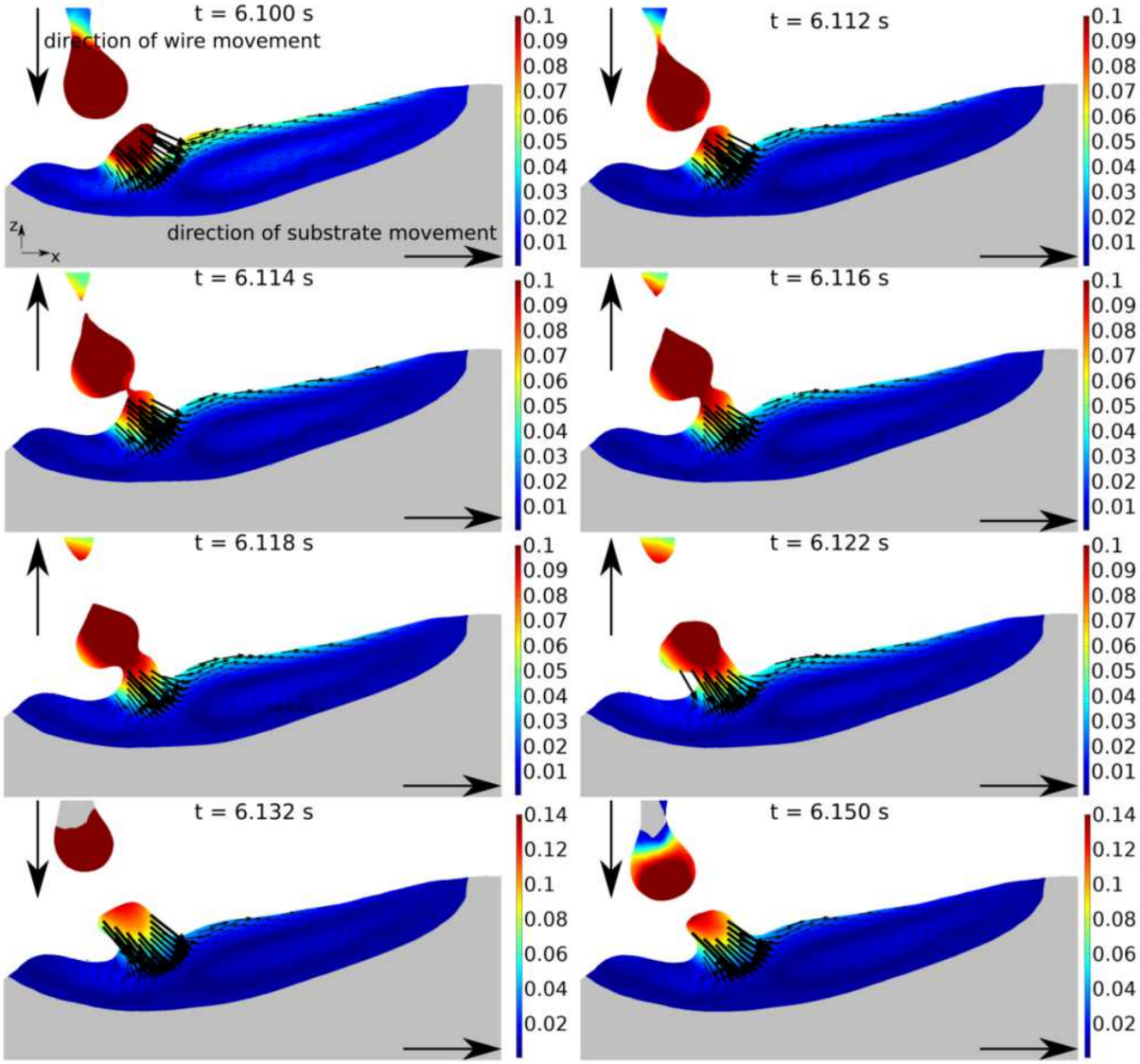

Fig. 5 – Longitudinal cross-sectional view (xz plane) of the fluid velocity field during metal transfer (in $m.s^{-1}$)

In Fig. 6, the dimensions of the melt pool are analysed and then compared with the experimental data for the first layer in order to validate the consistency of the model (Fig. 7, Fig.8). The numerical melt pool length is estimated at 13.7 mm, which is in agreement with the experimental value of 13.2 mm. In addition, the height of the melt pool estimated by the model is 3.1 mm, which is close to the height obtained during the experiment, which was 2.9 mm. However, the model overestimates the width of the deposit which is found to be 9.3 mm whereas the experimental width is only 6.1 mm for the first layer at the top surface of the substrate (Fig. 7). A plausible explanation could be that the model does not take into account the wettability phenomenon. Indeed, the level set method defines a single continuous interface for liquid/gas and solid/gas transitions. The liquid/gas interface can move freely with the fluid flow and the solid liquid/gas interface is stopped with the Darcy condition (eq.12). But numerically, the continuous curvature of the interface between solid and liquid does not allow the correct description of the wettability phenomena and the contact angle. During computation, the numerical diffusion implies an unwanted shift of the contact angle leading to a wider geometry.

In addition, the Marangoni effect should be added to have a more realistic behaviour, as shown by the experiments of Ahsan [21]. A relevant modelling of these phenomena will require more experimental data.

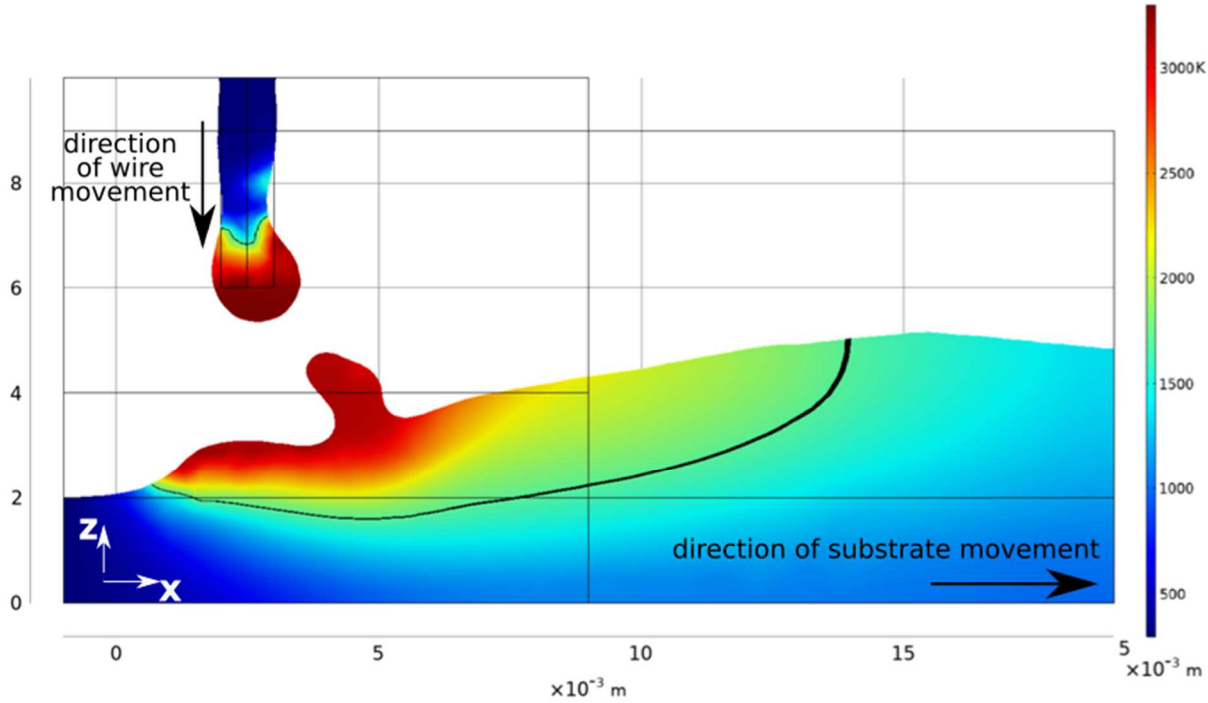

Fig. 6 – Longitudinal cross-sectional view (xz plane) of temperature field (in K) and isotherm of melting temperature (black line) at t = 6.7 s

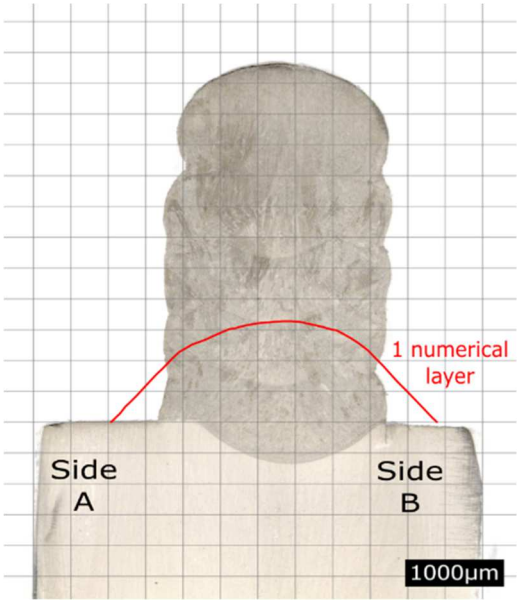

Fig. 7 - Comparison of the numerical shape of the first deposit (in red) with the experimental macrograph of 5 layers

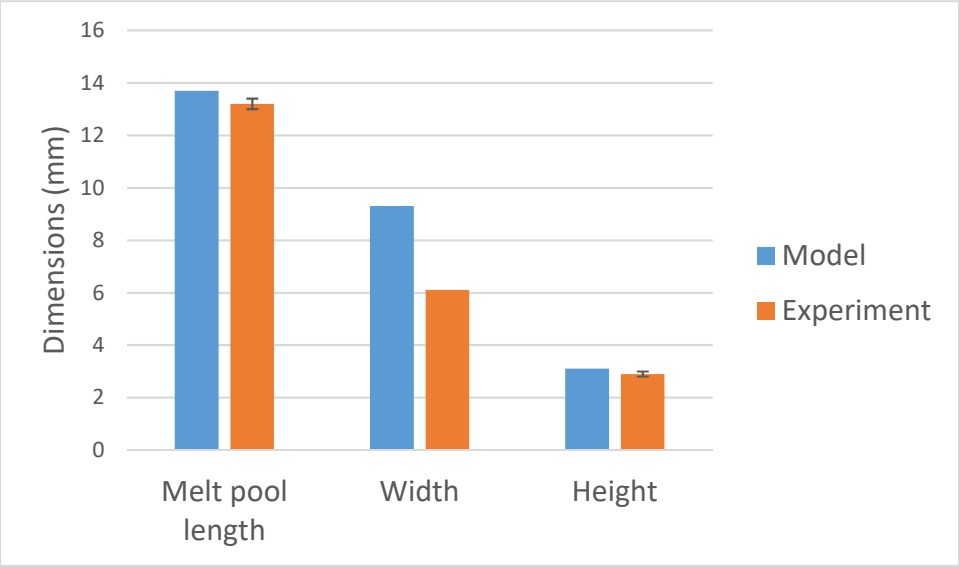

Fig. 8 - Comparison of the melt pool dimensions obtained by model and experiment

This multiphysics model can also be used to investigate the evolution of the electric current path during the build-up of the part. Fig. 9 highlights that the preferential path of current is through the drop, which is logical since steel is a better electrical conductor than argon. This sequence of images shows that the electric current lines are strongly affected by the dynamic topological change of the melt pool during droplet detachment. The constriction of the current lines can be observed when the droplet adopts an elongated shape. This constriction is also associated to an increase of the arc temperature in this region. Note that the current distribution plays decisive role in the fluid flows via the electromagnetic forces, but also on the thermal phenomena via the Joule effect.

One of the features of the CMT process is that the electrical signals are cyclic. Fig. 10 shows the voltage waveforms calculated by the model for four metal transfer cycles. With the help of Fig. 9, it can been observed that the voltage becomes zero when the wire is in contact with the melt. Then, when the wire is feed forward, the voltage increases rapidly and reaches a value around 35 V. During the retraction of the wire, the voltage decreases and becomes zero once again and a new cycle appears. The evolution of the voltage calculated by the model is consistent with the electrical cycles measured by Chen et al. [36].

These electrical variations have also an impact on the temperature field of argon (Fig. 9). When the wire is approaching the melt pool, the tension decreases, and therefore the temperature also, reaching values around 3000 K. The maximum temperature of the argon, estimated by the model at 9000 K, is reached when the wire is in the high position.

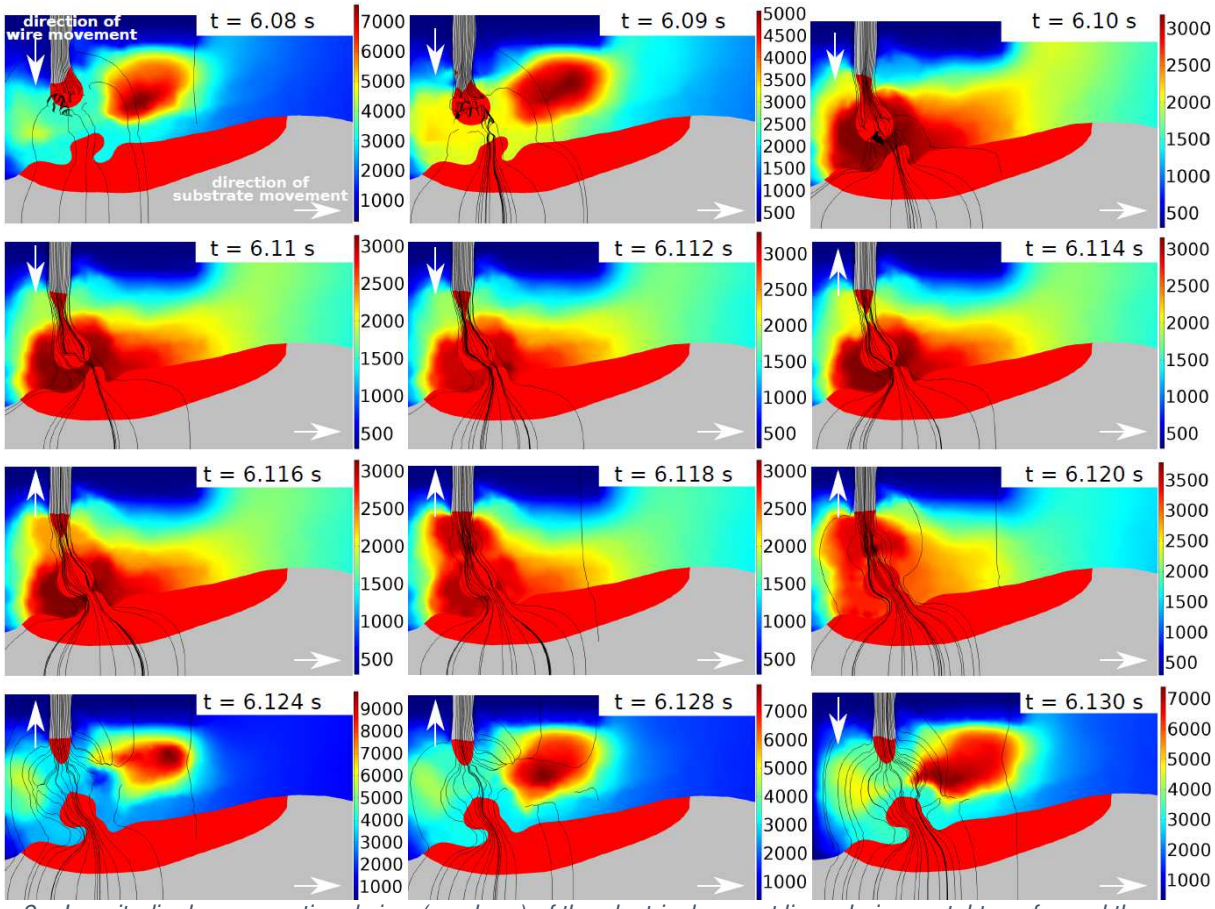

Fig. 9 – Longitudinal cross-sectional view (xz-plane) of the electrical current lines during metal transfer and the temperature field (in K) in the arc. The melting zone is represented in red.

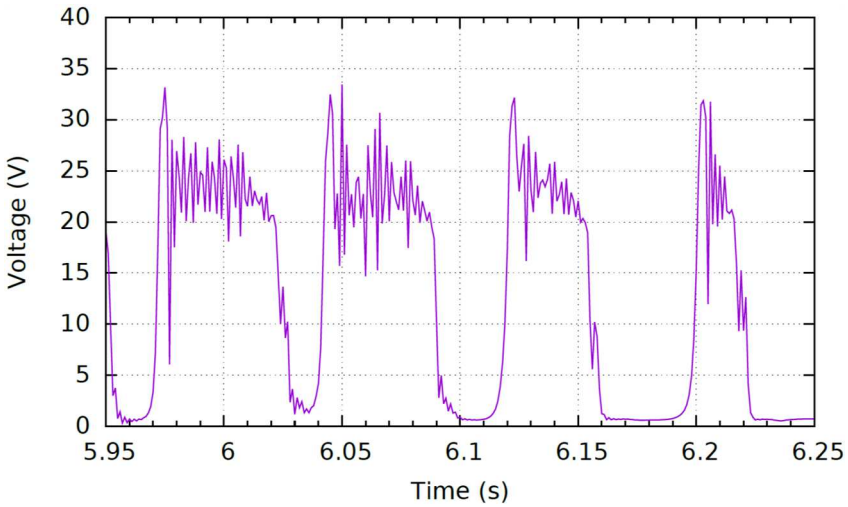

Fig. 10 -Evolution of the voltage during four metal transfer cycles.

4. Conclusions

In this study, electromagnetic, heat transfer and fluid flow in the plasma and the melt pool are investigated through a transient 3D model to simulate a WAAM process. All the main driving phenomena are included in the model. The use of the level set method makes it possible to analyse the complex mechanisms of droplet detachment during a CMT process. The model reproduces the mechanical motion of the wire. Indeed, the feeding direction is reversed when the voltage becomes zero at the time the wire dips in the molten pool. The simulation results exhibit good agreements with experimental data in terms of melt pool dimensions. This model, although it could be improved, enables the simulation of the forward and backward motion of the wire, the droplet detachment, the growth of the melt pool and the evolution of the temperature and fluid velocity during all the build-up of the first layer. These first numeral results demonstrate for the first time the feasibility of solving all the equations in the wire, plasma and deposit with a 3D complete CMT model. The development of this model remains to be pursued to obtain a better agreement between model and experiment. In the absence of precise experimental data concerning some model input parameters, such as changes in wire speed, intensity, and voltage over time via synergies, assumptions have been made. More comprehensive experimental measurements would help refine these assumptions. This model also made it possible to show the limits in terms of computation time. It takes 15 days to simulate only 6 s. It is therefore unthinkable to simulate the build-up of a whole part using such model. An approach coupling this multiphyiscs model at the scale of the melt pool with a simplified model at the scale of the workpiece will be considered in the future.

5. Acknowledgments

The authors are grateful to Pascal Paillard, Lauriane Guilmois and Paul Daheron from the Institut Matériaux Jean Rouxel (IMN – UMR 6502– Polytech Nantes, France) for their scientific and technical support during our experimental investigations.

6. References

[1] L. A. Jones, T. W. Eagar, and J. H. Lang, ‘A dynamic model of drops detaching from a gas metal arc welding electrode’, *J. Phys. Appl. Phys.*, vol. 31, no. 1, pp. 107–123, Jan. 1998, doi: 10.1088/0022-3727/31/1/014.

[2] L. A. Jones, T. W. Eagar, and J. H. Lang, ‘Magnetic forces acting on molten drops in gas metal arc welding’, *J. Phys. Appl. Phys.*, vol. 31, no. 1, pp. 93–106, Jan. 1998, doi: 10.1088/0022-3727/31/1/013.

[3] H. G. Fan and R. Kovacevic, ‘A unified model of transport phenomena in gas metal arc welding including electrode, arc plasma and molten pool’, *J. Phys. Appl. Phys.*, vol. 37, no. 18, pp. 2531–2544, Sep. 2004, doi: 10.1088/0022-3727/37/18/009.

[4] J. Hu and H. L. Tsai, ‘Heat and mass transfer in gas metal arc welding. Part I: The arc’, *Int. J. Heat Mass Transf.*, vol. 50, no. 5–6, pp. 833–846, Mar. 2007, doi: 10.1016/j.ijheatmasstransfer.2006.08.025.

[5] J. Hu and H. L. Tsai, ‘Heat and mass transfer in gas metal arc welding. Part II: The metal’, *Int. J. Heat Mass Transf.*, vol. 50, no. 5–6, pp. 808–820, Mar. 2007, doi: 10.1016/j.ijheatmasstransfer.2006.08.026.

[6] Y. Ogino and Y. Hirata, ‘Numerical simulation of metal transfer in argon gas-shielded GMAW’, *Weld. World*, vol. 59, no. 4, pp. 465–473, Jul. 2015, doi: 10.1007/s40194-015-0221-8.

[7] Y. Zhao and H. Chung, ‘Numerical simulation of the transition of metal transfer from globular to spray mode in gas metal arc welding using phase field method’, *J. Mater.*

Process. Technol., vol. 251, pp. 251–261, Jan. 2018, doi: 10.1016/j.jmatprotec.2017.08.036.
[8] Y. Zhao and H. Chung, 'Numerical simulation of droplet transfer behavior in variable polarity gas metal arc welding', *Int. J. Heat Mass Transf.*, vol. 111, pp. 1129–1141, Aug. 2017, doi: 10.1016/j.ijheatmasstransfer.2017.04.090.
[9] Y. Zhao and H. Chung, 'Influence of power source dynamics on metal and heat transfer behaviors in pulsed gas metal arc welding', *Int. J. Heat Mass Transf.*, vol. 121, pp. 887–899, Jun. 2018, doi: 10.1016/j.ijheatmasstransfer.2018.01.058.
[10] Y. Zhao, P.-S. Lee, and H. Chung, 'Effect of pulsing parameters on drop transfer dynamics and heat transfer behavior in pulsed gas metal arc welding', *Int. J. Heat Mass Transf.*, vol. 129, pp. 1110–1122, Feb. 2019, doi: 10.1016/j.ijheatmasstransfer.2018.10.037.
[11] Y. Ogino, Y. Hirata, and A. B. Murphy, 'Numerical simulation of GMAW process using Ar and an Ar–CO2 gas mixture', *Weld. World*, vol. 60, no. 2, pp. 345–353, Mar. 2016, doi: 10.1007/s40194-015-0287-3.
[12] Y. Ogino, Y. Hirata, and S. Asai, 'Numerical simulation of metal transfer in pulsed-MIG welding', *Weld. World*, vol. 61, no. 6, pp. 1289–1296, Nov. 2017, doi: 10.1007/s40194-017-0492-3.
[13] X. Bai *et al.*, 'Numerical analysis of heat transfer and fluid flow in multilayer deposition of PAW-based wire and arc additive manufacturing', *Int. J. Heat Mass Transf.*, vol. 124, pp. 504–516, Sep. 2018, doi: 10.1016/j.ijheatmasstransfer.2018.03.085.
[14] Y. Ogino, S. Asai, and Y. Hirata, 'Numerical simulation of WAAM process by a GMAW weld pool model', *Weld. World*, vol. 62, no. 2, pp. 393–401, Mar. 2018, doi: 10.1007/s40194-018-0556-z.
[15] F. Hejripour, D. T. Valentine, and D. K. Aidun, 'Study of mass transport in cold wire deposition for Wire Arc Additive Manufacturing', *Int. J. Heat Mass Transf.*, vol. 125, pp. 471–484, Oct. 2018, doi: 10.1016/j.ijheatmasstransfer.2018.04.092.
[16] G. Xu, J. Hu, and H. L. Tsai, 'Three-dimensional modeling of arc plasma and metal transfer in gas metal arc welding', *Int. J. Heat Mass Transf.*, vol. 52, no. 7–8, pp. 1709–1724, Mar. 2009, doi: 10.1016/j.ijheatmasstransfer.2008.09.018.
[17] X. Zhou, H. Zhang, G. Wang, and X. Bai, 'Three-dimensional numerical simulation of arc and metal transport in arc welding based additive manufacturing', *Int. J. Heat Mass Transf.*, vol. 103, no. Supplement C, pp. 521–537, Dec. 2016, doi: 10.1016/j.ijheatmasstransfer.2016.06.084.
[18] S. Cadiou, M. Courtois, M. Carin, W. Berckmans, and P. Le Masson, 'Heat transfer, fluid flow and electromagnetic model of droplets generation and melt pool behaviour for wire arc additive manufacturing', *Int. J. Heat Mass Transf.*, vol. 148, p. 119102, Feb. 2020, doi: 10.1016/j.ijheatmasstransfer.2019.119102.
[19] F. Lago, J. J. Gonzalez, P. Freton, and A. Gleizes, 'A numerical modelling of an electric arc and its interaction with the anode: Part I. The two-dimensional model', *J. Phys. Appl. Phys.*, vol. 37, no. 6, pp. 883–897, Mar. 2004, doi: 10.1088/0022-3727/37/6/013.
[20] A. Traidia, 'Multiphysics modelling and numerical simulation of GTA weld pools', Ecole Polytechnique, 2011.
[21] Md. R. U. Ahsan, T. Kim, D. bong Kim, C. Ji, and Y.-D. Park, 'A Study on the Effect of Wire Composition on Welding with Gap and Offset in Cold Metal Transfer (CMT) GMAW', *J. Weld. Join.*, vol. 36, no. 5, pp. 12–18, Oct. 2018, doi: 10.5781/JWJ.2018.36.5.2.
[22] J. Mougenot, J.-J. Gonzalez, P. Freton, and M. Masquère, 'Plasma–weld pool interaction in tungsten inert-gas configuration', *J. Phys. Appl. Phys.*, vol. 46, no. 13, p. 135206, Apr. 2013, doi: 10.1088/0022-3727/46/13/135206.
[23] A. B. Murphy, M. Tanaka, K. Yamamoto, S. Tashiro, J. J. Lowke, and K. Ostrikov, 'Modelling of arc welding: The importance of including the arc plasma in the computational domain', *Vacuum*, vol. 85, no. 5, pp. 579–584, Nov. 2010, doi: 10.1016/j.vacuum.2010.08.015.

[24] M. Tanaka, H. Terasaki, M. Ushio, and J. J. Lowke, ‘A unified numerical modeling of stationary tungsten-inert-gas welding process’, *Metall. Mater. Trans. A*, vol. 33, no. 7, pp. 2043–2052, 2002.
[25] S. Osher and J. A. Sethian, ‘Fronts propagating with curvature-dependent speed: Algorithms based on Hamilton-Jacobi formulations’, *J. Comput. Phys.*, vol. 79, no. 1, pp. 12–49, Nov. 1988, doi: 10.1016/0021-9991(88)90002-2.
[26] M. Courtois, M. Carin, P. Le Masson, and S. Gaied, ‘Complete 3D heat and fluid flow modeling of keyhole laser welding and methods to reduce calculation times’, *Math. Model. Weld Phenom. 12*, 2018, doi: 10.3217/978-3-85125-615-4-01.
[27] E. Olsson and G. Kreiss, ‘A conservative level set method for two phase flow’, *J. Comput. Phys.*, vol. 210, no. 1, pp. 225–246, Nov. 2005, doi: 10.1016/j.jcp.2005.04.007.
[28] M. Khenner, A. Averbuch, M. Israeli, and M. Nathan, ‘Numerical Simulation of Grain-Boundary Grooving by Level Set Method’, *J. Comput. Phys.*, vol. 170, no. 2, pp. 764–784, Jul. 2001, doi: 10.1006/jcph.2001.6760.
[29] L. T. Cheng and Y.-H. Tsai, ‘Redistancing by flow of time dependent eikonal equation’, *J. Comput. Phys.*, vol. 227, no. 8, pp. 4002–4017, Apr. 2008, doi: 10.1016/j.jcp.2007.12.018.
[30] B. Lafaurie, C. Nardone, R. Scardovelli, S. Zaleski, and G. Zanetti, ‘Modelling Merging and Fragmentation in Multiphase Flows with SURFER’, *J. Comput. Phys.*, vol. 113, no. 1, pp. 134–147, Jul. 1994, doi: 10.1006/jcph.1994.1123.
[31] M. Tanaka and J. J. Lowke, ‘Predictions of weld pool profiles using plasma physics’, *J. Phys. Appl. Phys.*, vol. 40, no. 1, pp. R1–R23, Jan. 2007, doi: 10.1088/0022-3727/40/1/R01.
[32] C. S. Kim, ‘Thermophysical Properties of Stainless Steels’, 1975, Accessed: May 11, 2017. [Online]. Available: http://inis.iaea.org/Search/search.aspx?orig_q=RN:7236394.
[33] C. Y. Ho and T. K. Chu, ‘Electrical Resistivity and Thermal Conductivity of Nine Selected AISI stainless Steels’, THERMOPHYSICAL AND ELECTRONIC PROPERTIES INFORMATION ANALYSIS CENTER LAFAYETTE IN, CINDAS-45, Sep. 1977. Accessed: Jul. 08, 2019. [Online]. Available: https://apps.dtic.mil/docs/citations/ADA129160.
[34] M. I. Boulos, P. Fauchais, and E. Pfender, *Thermal Plasmas*. Boston, MA: Springer US, 1994.
[35] H. G. Fan, H. L. Tsai, and S.-J. Na, ‘Heat transfer and fluid flow in a partially or fully penetrated weld pool in gas tungsten arc welding’, *Int. J. Heat Mass Transf.*, vol. 44, pp. 417–428, Aug. 2000, doi: 10.1016/S0017-9310(00)00094-6.
[36] M. Chen, D. Zhang, and C. Wu, ‘Current waveform effects on CMT welding of mild steel’, *J. Mater. Process. Technol.*, vol. 243, pp. 395–404, May 2017, doi: 10.1016/j.jmatprotec.2017.01.004.

Graphical abstract:

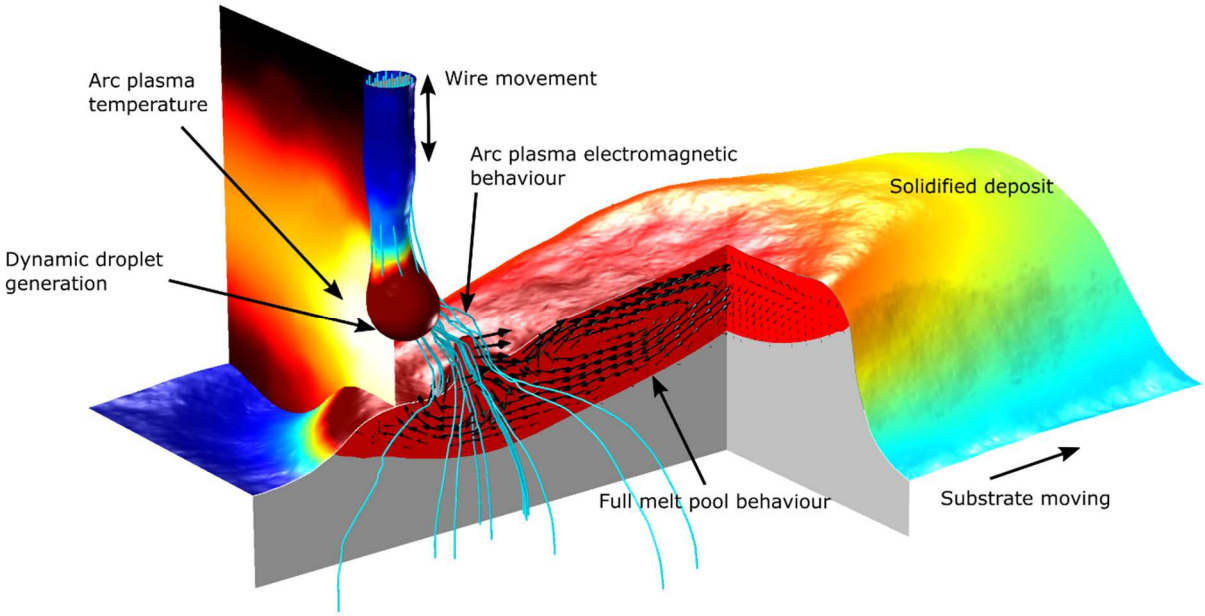

Highlights:

1- First complete multiphysics 3D model for Cold Metal Transfer (CMT)

2- Fully coupled model including arc, wire and melt pool with level set method

3- All the stages during forward and backward wire movement efficiently predicted

3- Optimization of computation time using a specific mesh strategy

5- Tool for a better understanding of synergic CMT process and material deposition

Video:

https://www.editorialmanager.com/addma/download.aspx?id=96956&guid=9bd10109-9428-4e2c-8663-46748edc8197&scheme=1